CHAPTER 8:
RESULTS FROM E896-SDDA

8.1 Detector performance results from E896

In this section, results from January 1997 and April 1998 beam runs are presented. To evaluate the detector efficiency, experimental results are compared to the expected hit occupancy calculated by using the ARC event generator and the GEANT simulation package to describe the geometry and the physics processes relevant to E896.

8.1.1 Hit parameters and distributions

Figure 8.1 shows the measured cluster amplitude as a function of drift distance. Each point corresponds to the most probable value of the amplitude distribution for a drift distance "bin". The error bars in this plot represent the RMS of the distribution for each drift distance bin and not the uncertainty of the most probable value. Figure 8.1 is similar to the laser signal amplitude distribution shown in figure 4.16. As expected the signal amplitude decreases with drift distance due to the electron cloud diffusion. Two sets of data are shown here, cluster amplitudes from data taken in January 1997 with a STAR2.7 detector, represented by the open squares, and cluster amplitudes from data taken in April 1998 measured with the STAR2.9 detector, represented by the solid circles. In January 1997 no measurements with drift distance above *21 mm* were recorded due to the lower operating bias on the detector. The readout electronics was designed to read the signal for a fixed amount of time, corresponding to the longest drift time at full drift field. With a lower HV value, the electron cloud drifts slower and

signal from the long drifts do not arrive in time for the readout, therefore, no data were recorded above a certain drift distance.

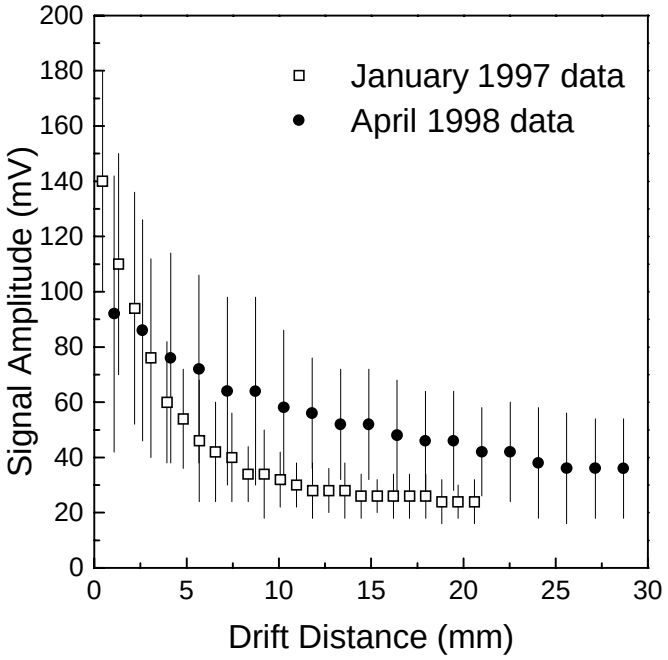

Figure 8.1: *Measured cluster amplitude (highest pixel) as a function of drift distance.*

The comparison between the results from the January 1997 and April 1998 runs shows that the 1998 data yield higher amplitudes. The same PASA gains were used in both data sets, therefore, the difference is attributed to the higher drift velocity used in 1998 and the differences in the detector design between the STAR2.7 and STAR2.9. This plot also confirms the expected improvement of the charge collection efficiency due to changes in the focusing region of the STAR2.9 detector.

Figure 8.2 shows the second moments "m_{11}" and "m_{22}" of the clusters measured in the January 1997 beam run, as a function of the drift distance. The plotted error bars correspond to the RMS of the width distribution for each drift

distance bin. The expansion of the electron cloud is obvious in both transverse and longitudinal directions. Based on figure 8.2, it can be noted that the electron cloud in the longitudinal direction expands slightly more than in the transverse direction. This expansion asymmetry is attributed to the existence of small drift non-linearities that can cause the electron cloud to diffuse more in the drift direction. However, the measured difference is small, indicating that drift non-linearity contributions are small, as expected.

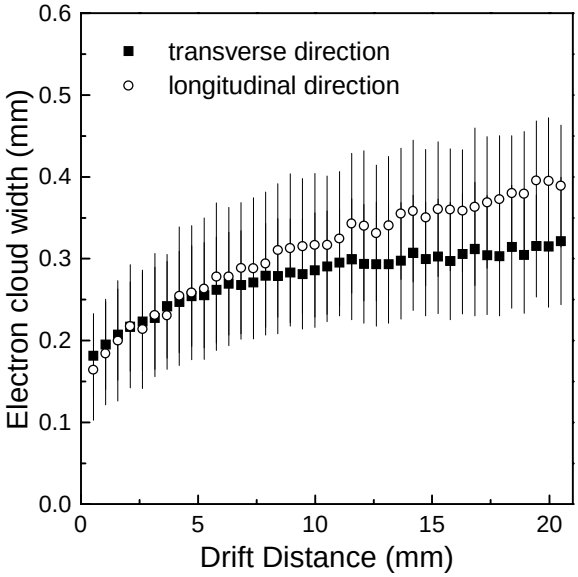

Figure 8.2: *Electron cloud size represented by the RMS values of the signal clusters in the transverse (anode) direction and in the longitudinal (drift) direction. Plots correspond to data measured with the STAR2.7 detector from the January 1997 beam run.*

Figure 8.3 shows the integrated charge of measured clusters as a function of drift distance based on data measured with the STAR2.7 detector in the January 1997 beam time. The points represented by solid squares include a correction due to the PASA response function. For increasing drift distance, the input widths of the electron cloud increases, which affects the shape of the output signal. For wider input signals, the contribution of the undershoot of the bipolar signal

increases, thus decreasing the total positive area of the output signal. The correction factor was measured by controlled charge injection in the PASA's. The summed ADC of the measured cluster is corrected by a factor that depends on the size of the cluster in the longitudinal direction.

$$Q_{corrected} = Q_{measured} \cdot \left(1 + 0.2\sqrt{m_{22}^2 - 0.7^2}\right) \quad \textbf{(8.1)}$$

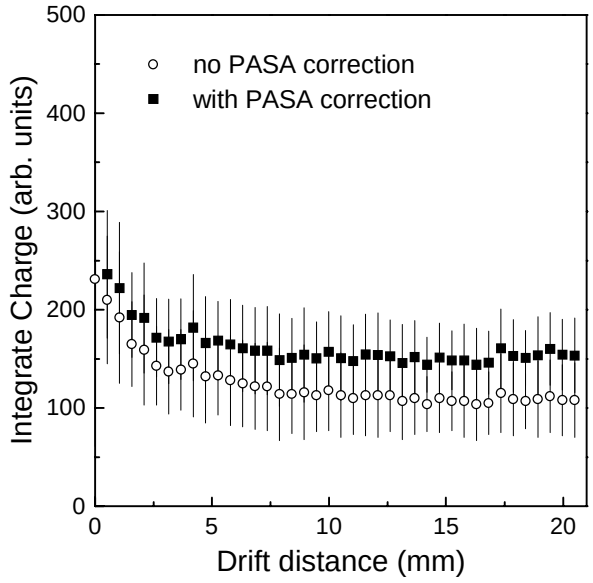

Figure 8.3: *Most probable value of the summed ADC (total charge) in arbitrary units for different drift distances. The open circles correspond to the "raw" integrated ADC vales and the solid squares correspond to the summed ADC values corrected for the PASA response function effect.*

Figure 8.3 indicates that for most of the drift distance, the collected charge is independent of the drift distance, as expected. However, a slight increase in the integrated charge is observed for short drift distances. There are a few possibilities that can cause such an increase. Inefficiency in measuring small clusters for short drift distances could cause a shift of the most probable value of the integrated charge distribution. For short drift distances, there is little spread of the electron

cloud therefore the signal is concentrated in a few pixels, instead of being distributed over many pixels. The cluster finder requirement of a minimum number of neighboring pixels above the lower threshold could lead to an inefficiency in finding these clusters. To solve this problem, a more complex cluster finder that considers different cluster shapes according to the drift position is required. Such a code is being developed for future SVT analysis.

The vertical axis in figure 8.3 corresponds to the integrated charge in arbitrary units. To obtain a calibration between the integrated ADC units and the ionized charge, it is necessary to study more carefully the total integrated charge. Such a study is discussed in section 8.2 of this chapter.

8.1.2 Hit efficiency

Figure 8.4 shows hits on a single detector superimposing 10 events of the April 1998 beam time. Approximately 60 hits per event were measured in each detector. The “butterfly shaped” guard area is visible on the right side of the detector. As mentioned in chapter 3, this inactive area corresponds to 6.4 % of the total detector. On the left bottom side of the detector, a noisy anode causes the artificial line of hits. False hits can be identified in the analysis at a later stage by parameters such as cluster size or integrated ADC value. As expected, the hit density increases towards the right side of the detector, in the direction where the beam and target were located. This effect is quantified in figure 8.5, where the hit density per event is plotted as a function of detector coordinate in the transverse (anode) direction and compared to a central Au+Au ARC simulation represented by the solid circles. The good agreement between the experimental data and the simulation indicates good hit efficiency.

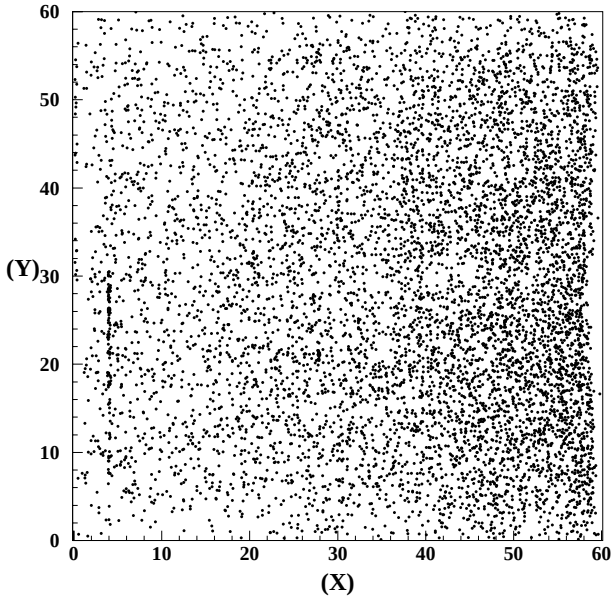

Figure 8.4: *Hit occupancy plot on one of the detectors from 10 events. Each dot corresponds to a hit measured in this detector.*

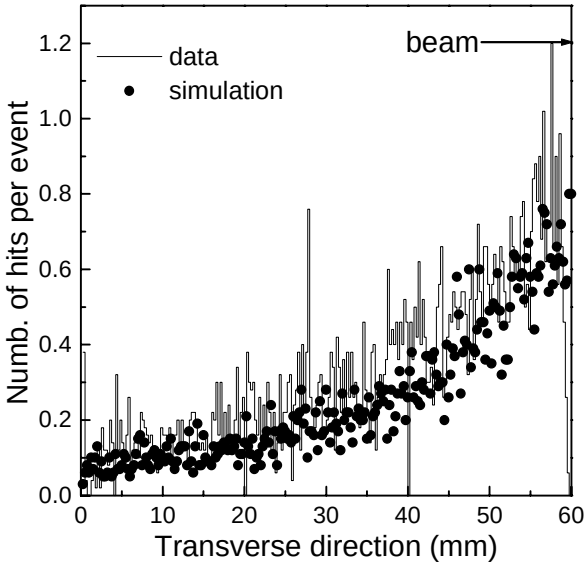

Figure 8.5: *Detector hit occupancy in the transverse direction (histogram), compared to the expected occupancy from the simulation (solid circles). The position of the beam and the reaction point is to the right side, in the scale of this plot, in accordance to the increasing occupancy towards the right side of the detector.*

Figure 8.6 shows the hit occupancy per event in the longitudinal (drift) direction and the comparison to the expected occupancy distribution based on ARC. A higher density of hits in the center of the detector in the longitudinal direction is expected and reflects the relative location of the beam axis. The experimental distribution shows a slight shift of the highest hit density towards the bottom side of the detector (position *20 mm* in the scale used in figure 8.6). That is in accordance with observations from the beam position monitors during the experiment. The beam was slightly offset compared to its nominal location. In general though, the agreement in the absolute number of hits between data and simulation allows the conclusion that the detector measures central Au+Au collision occupancies with only little inefficiencies. The simulation was performed assuming an event cut on the upper 20% of the geometrical cross section, which is in accordance with the E896 trigger condition.

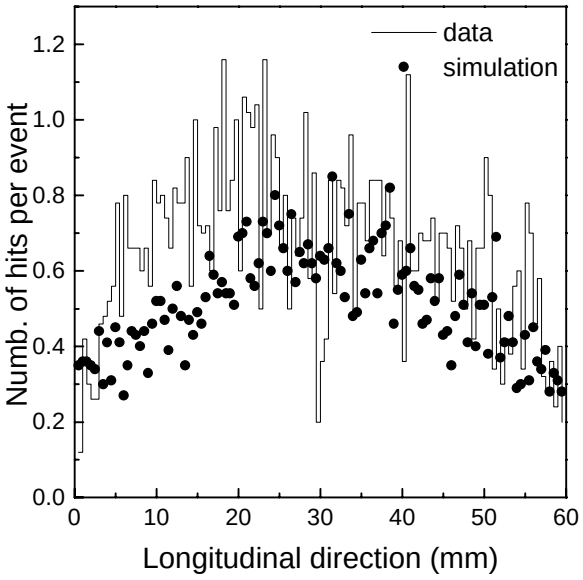

Figure 8.6: *Detector hit occupancy in the longitudinal direction (histogram), compared to the expected occupancy from the simulation (solid circles).*

8.2 Energy loss studies

8.2.1 The basics of charged particle energy loss

The average energy loss of a particle traversing a solid material is calculated by the Bethe-Bloch equation (see chapter 2.1.4). Due to the high number of collisions that the particle undergoes, which leads to statistical fluctuations, the total amount of energy lost by a particle is better described by a distribution function.

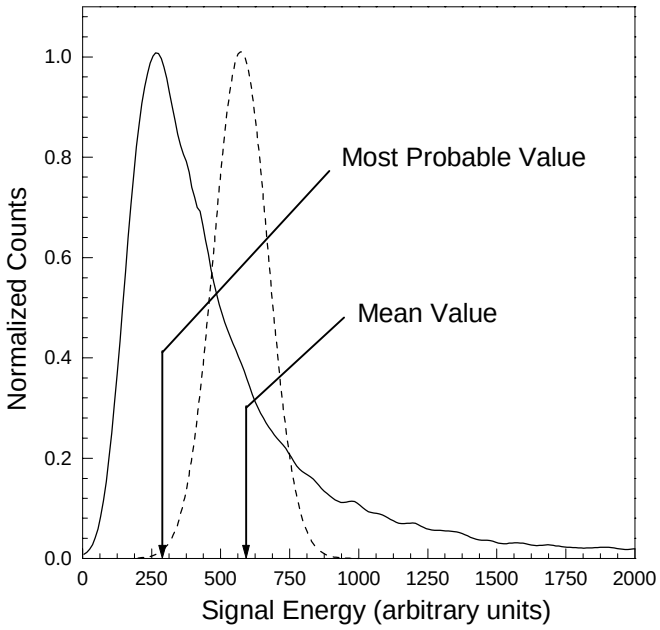

Figure 8.7: *The Landau distribution that describes the energy loss distribution in thin absorbers.*

In thick absorbers, the number of collisions is sufficiently large to describe the energy loss distribution by a Gaussian approximation (Statistic's Central Limit Theorem). For thin layers, such as in the case of semiconductor detectors (with average thickness of ~$300\mu m$), the fluctuation of energy deposition by passing radiation is better described by a Landau distribution [ref. 8.1]. Figure 8.7 illustrates the general shape of the Landau distribution, which is asymmetric with a long tail towards higher energy losses. This long tail can be understood

considering that in thin layers, high-energy transfer is reduced, therefore, the most probable energy loss is lower than the mean value. In addition, there is also the possibility of high momentum transfer collisions, which produce high-energy Delta electrons that contribute to the long tail of the distribution. The mean value and the most probable value, shown schematically in figure 8.7, parameterize the distribution. It is noteworthy that the two values converge to the same value in the limit of a Gaussian distribution. The mean value is extremely sensitive to the number of counts in the tail of the distribution, and therefore it is very difficult to quantify to a high precision, especially in the case of thin detectors.

The Landau calculation makes a few assumptions. It considers that the maximum permitted energy transfer is infinite. The individual energy transfer is sufficiently large such that the ionized electrons are treated as free. Small energy transfers are ignored and the velocity of the incident particle is not affected by the collisions. A more accurate distribution was implemented by Vavilov [ref. 8.2], by introducing a kinematic limit on the maximum transferable energy in a single collision.

8.2.2 Energy loss measurements and calibration

The dotted line in figure 8.8(a) shows the distribution of the integrated charge of all clusters recorded in the January 1997 run. The shape of the energy spectrum exhibits the characteristics of a Landau distribution. The solid line histogram represents the energy distribution after the correction for the PASA response function (equation 8.1). Figure 8.8(b) shows the same histogram (PASA corrected), on a logarithmic scale.

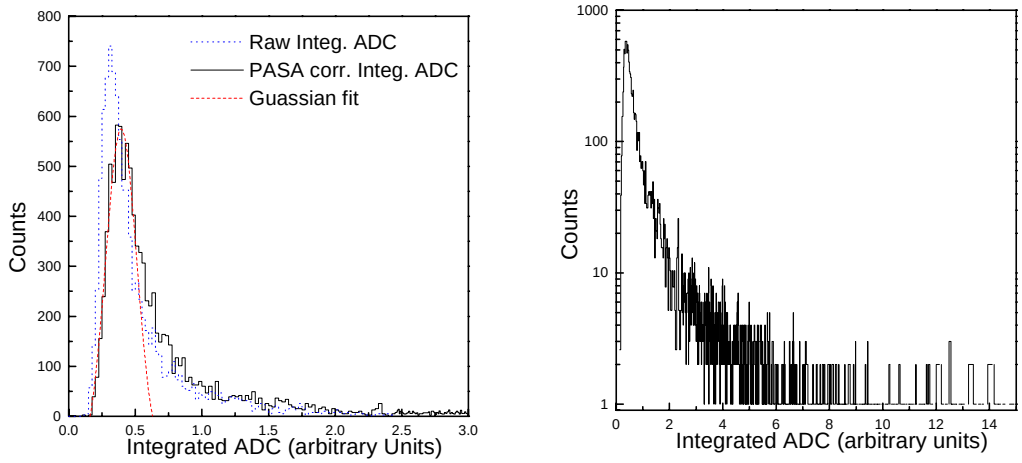

(a) **(b)**

Figure 8.8: *(a) Raw integrated ADC spectrum and corrected for the effects of the PASA response function. A gaussian distribution was fitted to the peak of the most probable value. (b) PASA corrected integrated ADC in a logarithmic scale.*

A calibration of the measured ADC values to an energy scale (in electron-volts) was obtained by comparing the experimental energy loss data with the mean energy deposition from the Bethe-Bloch equation (equation 2.20) and considering the Landau and Vavilov distributions. The expected enegy spectrum was simulated utilizing ARC generated particles and the GEANT simulation frame (section 7.4). For the comparison between the experimental data with the simulated energy spectrum, the following considerations were made:

- In a *300 μm* thick silicon, the most probable value of the energy loss by a MIP particle is around *90 keV*.

- The experimental energy spectrum is the result of the sum of Landau distributions for particles of different mean energies. From the simulated momentum distribution, most of the particles that traversed the detector are expected to be minimum-ionizing (MIP) particles. Under that assumption, it is reasonable to consider that most of the hits in the peak of the distribution are

due to MIP particles. Thus, to adjust the experimental data to the simulated curve, one should consider mostly the peak region of the most probable value.

- Due to the minimum cluster size and ADC thresholds imposed by the cluster finder algorithm, there could be an inefficiency in finding clusters with very low integrated charge. Therefore, the low energy end of the spectrum should not be considered for the fit.

- Another important fact that should be considered is the broadening of the energy loss distribution caused by the noise fluctuation of the ADC values. Each ADC pixel has an intrinsic noise of approximately *5mV* (section 7.4.1). Considering no correlation between different pixels, and an average cluster size of 30 pixels, the average error of the integrated charge value is then given by: $5mV \cdot \sqrt{30} \cong 27mV$, which corresponds to *10%* of the ADC counts of the most probable value of the distribution. To account for this error, the GEANT energy loss spectrum was smeared by *10%*, which increased slightly the width of the energy spectrum.

Figure 8.9(a) shows the region near the peak that was considered to compare the calculated energy loss spectrum to the experimental data. In the Landau distribution, the low energy side of the peak can be described by a gaussian fit, as shown by the dashed curve. The comparison between the experimental spectrum and the GEANT calculated spectrum results in the following calibration equation:

$$Q(MeV) = 0.1102 \cdot Q(ADC\ counts) + 0.049 \qquad \textbf{(8.2)}$$

The wide range of the energy spectrum (figure 8.9b) shows that signals with integrated charge from 60 keV to 1500 keV are measured, proving that both the detector and the corresponding electronics, have good dynamic range for

measuring high ionizing particles. Furthermore, the signal shape of the "large hits" exhibits no evidence of any saturation.

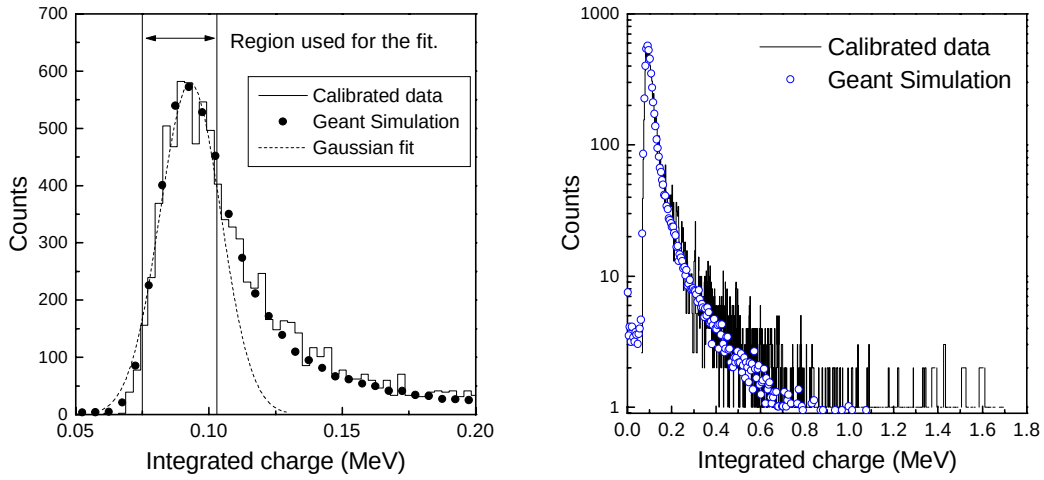

(a) **(b)**

Figure 8.9: *Integrated charge spectrum compared to the GEANT simulated energy loss spectrum. The data was calibrated to the simulation.*

In a more detailed comparison, data and simulated spectra show good agreement in the low energy region (below 0.3 MeV), however, in the high energy region the experimental data seems to indicate a higher number of entries.

One possible contribution to the enrichment of the high energy tail of the distribution are hits made by low momentum particles. Based on the Bethe-Bloch equation and considering a *300 μm* thick silicon, a singly charged particle needs to have a momentum lower than 0.2 GeV/c in order to deposit 1500 keV. However, assuming that the utilized ARC particle generator can predict reliably the momentum distribution of the most abundant particles (pions, protons and electrons) this contribution should already be accounted for in the simulated spectra.

The other possible contribution to the tail of the energy spectrum is due to larger clusters of particles (deuterons, tritons, 3He and alpha clusters) which are not included in the ARC simulation code. These cluster particles can be non-interacting fragments originated from the target or the product of coalescence mechanism [ref. 8.3, 8.4] of protons end neutrons generated in the reaction. The later is more probable in central collisions.

The study of coalescence cross-sections and momentum distribution of large clusters in heavy-ion collisions is very interesting to understand the reaction dynamics. The comparison shown in figure 8.9(b) could provide a method to study coalescence cross-sections however, the data taken in January 1997 do not yield sufficient statistics for such studies. In addition, the lack of momentum information does not allow to determine if the “large hits” are generated by low momentum particles or by multiple charged particles. The April 1998 data taking run will provide measurements from several detector layers (15) which provides better energy resolution for each particle track in addition to its momentum information. Hence dEdx versus particle momentum can be used for particle identification.